European Journal of Mechanics / A Solids 99 (2023) 104942

Contents lists available at ScienceDirect

European Journal of Mechanics / A Solids

journal homepage: www.elsevier.com/locate/ejmsol

An adhesion study in Ni and Cu nanocontacts from a molecular dynamics perspective

S. González-Tortuero, M.A. Garrido, J. Rodríguez *

DIMME, Grupo de Durabilidad e Integridad Mecánica de Materiales Estructurales, Universidad Rey Juan Carlos. C/ Tulipán, s/n. 28933 Móstoles. Madrid. Spain

ARTICLE INFO

Keywords:
Molecular dynamics
Contact mechanics
Adhesion
Nanoindentation

ABSTRACT

In this work, the effects of adhesion in nanoscale indentation tests with copper and nickel samples indented with a spherical diamond tip have been studied. The tests have been simulated by molecular dynamics, initially selecting the appropriate potentials according to the pair of materials put in contact. The force-displacement curves of a complete cycle of loading and unloading have been determined and a procedure for the simultaneously determination of the indentation modulus of elasticity and the adhesion energy of inelastic indentations have been developed. Likewise, a critical evaluation of the contact models available in the literature has been carried out, assessing their suitability for the cases analysed.

1. Introduction

The performance of micro and nanoelectromechanical systems (MEMS/NEMS) is very sensitive to the conditions of the contacts between their parts. These devices can benefit considerably from atomic layer deposition techniques, optimizing their working thanks to the application of coatings. Thin metal films deposited on devices, switches, sensors, and actuators are used to form conductive contacts and reflective coatings. Furthermore, these metallic coatings can also be used as structural layers to improve the mechanical response, that is, to increase the wear resistance or reduce the static friction of gears and actuators (Bhushan, 2003, 2007; Tichy and Meyer, 2000). In other devices such as thermal actuators, capacitors in RF MEMS, optical switches, micromirror hinges, micromotors, and other miniaturized machines, thin films are subjected to mechanical loads. The appropriate evaluation of the mechanical properties at this scale plays an essential role for the advance of MEMS and NEMS (Chasiotis et al., 2007; Eberl et al., 2006; Tuck et al., 2005). Additionally, many innovative MEMS applications require materials that exhibit simultaneous functionalities while maintaining mechanical integrity.

Ni-based alloy films have been electroplated in MEMS/NEMS to provide high strength and electrical conductivity. Gi-Dong et al. (Gi-Dong Sim et al., 2017) deposited single-phase solid solution nickel-molybdenum-tungsten (Ni–Mo–W) films by means of high-power, direct current (dc) sputter deposition. They developed an optimal combination of exceptionally high tensile strength with thermal and mechanical stability by sputtering Ni–Mo–W, which turned out to be a promising solution to broaden the application of MEMS.

Cu thin films are commonly used in advanced microelectronics (Song Tao and D Y Li, 2006). Their mechanical properties and microstructure features, such as grain boundary and crystallographic texture, can significantly influence the performance of electronic devices (Cao et al., 2009). Cu films have been deposited to produce MEMS/NEMS with high conductivity, low friction and high wear resistance (Geetha et al., 2013; Hu et al., 2020; Kang et al., 2002; Teh et al., 2001; Zhang et al., 2003).

Knowledge of surface interactions at micro and nanoscale, such as friction, adhesion, meniscus forces and surface tension is fundamental to produce reliable and durable MEMS and NEMS. (Bhushan, 2008; Li et al., 2003). These interactions can be altered by the formation of adsorbed layers, surface chemistry or the effect of lubricants added to improve the tribological performance of devices (Chandross et al., 2008; Dai et al., 2016; Stephan et al., 2018). For example, the addition of surfactants to interface materials may improve the heat dissipation efficiency of microelectronic surfaces in contact (Guo et al., 2019; Y. Y. Guo et al., 2020; Liu et al., 2021) selected several surfactants to modify the coal surface structure to modulate its wettability. A model of surfactant adsorption on coals was reported. This research was completed with a molecular dynamics study to simulate the adsorption process of different surfactants on coal surfaces. The adsorption of complex molecules on surfaces have recently become the subject of intense research because it could improve our ability to control essential interfacial properties in a wide variety of problem, including adhesion, wetting and

* Corresponding author.
E-mail address: jesus.rodriguez.perez@urjc.es (J. Rodríguez).

https://doi.org/10.1016/j.euromechsol.2023.104942
Received 11 October 2022; Received in revised form 10 January 2023; Accepted 7 February 2023
Available online 9 February 2023

nano-wetting, biomolecular recognition and self-assembly. Yang et al. (Yang and Zhao, 2007) carried out molecular dynamics to study the adsorption of peptide with Ni, Cu and Au (1 0 0) surfaces in order to analyze their interactions. For all these reasons, the characterization of the interactions between surfaces constitutes a crucial investigation to understand the properties and behaviour of nanodevices.

Nanoindentation is one of the few alternatives that has been used to determine mechanical properties of thin films and bulk materials at the nanoscale. The mechanical properties most frequently measured using this technique are elastic modulus and hardness (Palacio and Bhushan, 2013; Tricoteaux et al., 2010), but contact models based on continuum mechanics are needed to analyze the experimental data. The Hertz elastic solution (Wang and Zhu, 2013) describes the contact behaviour between a sphere and a flat surface relatively well and is widely used to explain the mechanical response of materials and coatings at macro and microscale (Z. Z. Guo et al., 2020; Herbert et al., 2001; Song and Komvopoulos, 2013; Tang and Arnell, 1999). The Hertz's contact model has also been used to determine properties at the nanometric and atomic scales. Kang et al. (2012) estimated the effective radii of a spherical nanoindenter at various indentation depths using Hertz elastic contact theory and residual indentation imprints from atomic force microscopy (AFM) profiles. In this study, they programmed the nanoindentation tests on fused silica, Al, Cu, Ni, and steel samples. Other works also reported nanoindentation tests at the nanometric and atomic scales using the Hertz contact model (Buchs et al., 2009; Jeong et al., 2021; Wu et al., 2016).

However, the mechanical response at macro and nanoscale can be completely different (Fincher et al., 2020). Apart from the anisotropic nature of polycrystalline metals, as the scale decrease, the adhesion effects, normally negligible at the macroscale, begin to be decisive. The interactions between the asperities of the surfaces in contact are significantly affected by these phenomena, requiring modifications in the Hertz model to provide reliable results. There are not many studies where adhesion is considered in the analysis of nanoindentation results in metallic materials. Morales-Rivas et al. (2015) studied the nanomechanical properties and deformation mechanisms of nanostructured bainite by nanoindentation with AFM. They reported adhesion effects between the sample and the tip, but they simply applied the Hertz model (Hertz, 1896; Johnson, 1985), which does not take this issue into account. Bigl et al. (2016) studied the effect of residual inorganic elements on the local plastic deformation of two different Cu films. For this investigation, they carried out nanoindentation tests with sharp indenters, but again adhesion was ignored.

There are some works where adhesion has been considered in the study of contact between rough surfaces, or in the analysis of friction in nanoindentation tests (Dai et al., 2020). Lin et al. (2019) studied the influence of surface roughness on adhesion of Cu thin films with different thicknesses. They obtained the indentation force-displacement curves by AFM. To illustrate the effect of roughness, they carried out a theoretical and simulation analyses of the contact based on the Johnson-Kendal-Roberts model (JKR) (Johnson et al., 1971). Birleanu et al. (2016) analysed the effect of the thickness on the nanomechanical and nanotribological performance of thin films of Cr, Ni, Ti and Pt. They performed AFM nanoindentation tests using a Berkovich tip, determining the work of adhesion with two theories of adhesion between elastic bodies: Derjaguin-Muller-Toporov (DMT) (Derjaguin et al., 1975) and JKR. Liu et al. (2006) studied the elastic adhesive contact with the continuous free Galerkin-finite element (EFG-FE) coupling method. A numerical simulation between a microelastic cylinder and a rigid half-space was done. The adhesive contact characteristics of three metals (Al, Cu, and Fe) at different values of the Tabor parameter μ (Tabor, 1977), from 4.04 to 8.12, were studied. In that work, the adhesive force distribution of the Dugdale model was used in the analyses.

Borodich and Galanov (Borodich and Galanov, 2008; Perepelkin et al., 2019) introduced a procedure that analyses stable data for the elastic stage of spherical indentation by making use of the method of regularization of general ill-posed problems to consider experimental uncertainties. They considered roughness of contacting surfaces, surface chemistry, wear of depth sensing indentation probe, chemical modification of its surface or dust particles.

The Borodich and Galanov method needs a previously selected contact model (JKR or DMT) to be defined by an analytical equation. However, this equation is not available when using a more general contact model, such as the Maugis transition theory. The Borodich and Galanov method can help to interpret those experiments in which the contact is well described by the JKR or DMT models, but it does not help to decide which is the best contact model in case it is not known in advance.

Experimental adhesion studies on a truly atomic scale are extremely complex. To the authors' knowledge, Jacobs and Carpick (2013) obtained one of the few contact area measurements using an AFM inside a transmission electron microscope (TEM). Although the reported contact area data had a considerable uncertainty and basically provided a 2D image of the contact surface, they were good enough to be used by Chen (2020) in comparisons with contact models based on continuum mechanics and molecular dynamics simulations. Difficulties in explaining with continuous models the difference between the loading and unloading branches in an atomic-scale indentation test were also revealed. This aspect is not yet resolved.

Parallel to the development of nanoindentation techniques, numerical methods are becoming increasingly relevant as alternative tools to study the behaviour of materials under experimental conditions that are very difficult and expensive to reproduce (Wan et al., 2021). Molecular Dynamics (MD) simulations are of increasing relevance to understand the indentation process at small length scale. Hansson et al. (Hansson, 2015) carried out simulations of spherical nanoindentation on copper with a 3D molecular dynamics approach. The thin Cu coating was simulated using an embedded-atom method (EAM) potential, consisting of a pairwise repulsive part and an attractive part with specific cut-off radii. (Holian and Ravelo, 1995). They concluded that in a Cu nanocoating the crystallographic orientation strongly influences the elastic and plastic behaviour. Hu et al. (2015) studied the anisotropy in crystallographic Ni substrates with (001), (011) and (111) orientations. They analysed the defect nucleation and the evolution of hardness and Young's modulus by MD simulations They reported values of Young's modulus of 190.5, 240.7 and 289.1 GPa for Ni (001), (011) and (111) orientations, respectively.

MD has not only been used to evaluate the mechanical properties of materials. Hansson (2016) analysed the effect of surface roughness on the elastic and plastic properties of thin copper coatings. Nair et al. (2008) investigated the effect of thickness on the indentation process of Ni thin films with embedded atom method (EAM) interatomic potentials.

Undoubtedly, one of the greatest possibilities offered by MD is the study of adhesion during indentation. Zhu et al. (2020) studied the effect of surface tension on the adhesive contact between a rigid sphere and an elastic half-plane where the adhesive interactions were dominated by the Dugdale laws. They reported a solution for the total force and penetration depth under adhesive contact with existence of surface tension. Shen et al. (Shen and Sun, 2010) used MD to study the indentation and friction responses of a spherical diamond tip in contact with a flat Cu substrate at atomic scale. They analysed the force-displacement indentation curves by combining the Hertz and JKR models. They reported that the contact radii of indentations, calculated from the MD simulations, deviate from the predictions of the continuum theory. These deviations varied with the atomic structure at the tip surface, the radius of the tip, and the normal load. They found that MD results were larger than the JKR predictions in the attractive region.

Li et al. (2015) developed a MD simulation to investigate the response of deformable Cu substrate under spherical indentations considering material anisotropy and adhesion. They studied the contact force as a function of the indentation depth by comparing MD results

with Hertz, JKR and DMT solutions, and concluded that none of the continuum mechanics-based models could correctly predict contact behaviour.

As indicated in the previous paragraphs, although work has been done considering adhesion in atomic-scale indentation tests, many questions remain to be solved and much more research is needed that systematically combines experimental results, continuous models and MD simulations.

This work is a step in that direction and its main objective is to study the behaviour of thin layers of Cu and Ni during an indentation process at the atomic scale and evaluate the adequacy of the different continuous models to describe this process. For this, MD simulations will be generated with spherical diamond tips and Cu and Ni substrates. The corresponding force-displacement curves will be compared with the predictions of contact models available in the literature, including Hertz, JKR, DMT and Maugis-Dugdale (Maugis, 1992), trying to find the best description of this process. The developed procedures provide the Young's modulus and the adhesion work in Ni–C and Cu–C nanocontacts.

2. Methodology

In this section, a detailed description of MD simulations is presented. In addition, an explanation is given to consider the adhesion effect during the indentation process in the Cu–C and Ni–C systems. Finally, a numerical procedure is developed that allows obtaining the elastic modulus and the adhesion properties in those cases where this phenomenon is relevant.

2.1. Simulation model

Molecular dynamics simulations have been carried out by using the open-source code Large-scale Atomic Molecular Massively Parallel Simulator (LAMMPS), developed by Sandia National Laboratories (http://lammps.sandia.gov). Simulations of the indentation process have been programmed using scripts on Ni and Cu, both with face centered cubic (FCC) lattice with a lattice constant of 3.62 Å and 3.52 Å, respectively. Both materials were chosen due to their wide use as nanocoatings for MEMS and NEMS devices, as described in the introduction section. Substrate sizes were 160 Å in the X and Z directions, and 90 Å in the Y direction. The indented surface was the (010) plane of Cu and Ni single crystals for all cases. The indenter was a spherical diamond probe with a tip radius of 20 Å (C atoms in the cubic diamond structure). This is a small tip but within the ranges reported in the recent bibliography (Mani et al., 2021; Shinde et al., 2022; Wang et al., 2019; Xu et al., 2021).

Several types of interactions must be taken into account during MD simulations. In particular, strong interactions within the same solid (associated to covalent or metallic bonds) must be distinguished from weak surface interactions between atoms of different solids where the Van der Waals forces are the dominant ones.

The strong interactions of Ni–Ni and Cu–Cu atoms within the substrate were described by the embedded atom method (EAM) potential (Daw and Baskes, 1984) where the total energy E_{tot} of this potential model can be calculated as:

$$E_{tot} = \sum F_i(\rho_{hi}) + \frac{1}{2}\sum_i \sum_{j(\neq i)} \varphi_{ij}(r_{ij}) \tag{1}$$

where ρ_{hi} is the electron density of the atom i, $Fi(\rho_{hi})$ is the energy of the embedded atom into the background electron density ρ, and $\varphi_{ij}(r_{ij})$ is the core–core pair repulsion between the atoms i and j separated through a distance r_{ij}. In this work, the values of the EAM potentials parameters reported by Foiles et al. (1986) were selected to simulate the Ni–Ni and Cu–Cu interactions, respectively.

The strong interactions C–C between atoms of the indenter were described by a Tersoff potential (Tersoff, 1988, 1989) where the energy is given by:

$$E_{Tf} = \frac{1}{2}\sum_{i\neq j} V_{ij} \tag{2}$$

and V_{ij} is taken to be:

$$V_{ij} = f_C(r_{ij})\left[f_R(r_{ij}) + b_{ij} f_A(r_{ij})\right] \tag{3}$$

Here i and j label the atoms of the system, r_{ij} is the length of the ij bond, f_C is a smooth cutoff function, f_R is a two-body repulsive term and f_A includes attractive three-body interactions. The sum in the formula extends over all neighbours of atom i within the cutoff distance. The values of the Tersoff potential parameters were taken from those reported by Tersoff for C-based systems (Tersoff, 1988).

The weak surface interactions between atoms of the indenter and atoms of the substrate (cases of Ni–C and Cu–C) were described by the Lennard-Jones (LJ) potential (Lennard-Jones, 1931). The LJ potential energy is defined in equation (A.3) included in the appendix. Since the values of the LJ potential constants for Ni–C and Cu–C interactions were not known, the Lorentz-Berthelot combining rules (LB) were used (Berthelot, 1898; Lorentz, 1881). Equations (4) and (5), were used to calculate the values of LJ potential:

$$\varepsilon_{ij} = \sqrt{\varepsilon_{ii}\varepsilon_{jj}} \tag{4}$$

$$\sigma_{ij} = \frac{\sigma_{ii} + \sigma_{jj}}{2} \tag{5}$$

Here, ε_{ii} and ε_{jj} are the depths of the potential well for atoms i and j and σ_{ii} and σ_{jj} are the distances at which the potential energy becomes zero for atoms i and j, respectively. According to the values reported in the literature for the weak surface interactions Ni–Ni and Cu–Cu (Che et al., 1998; Erkoç, 2001), the following parameters were finally applied: $\varepsilon_{Ni-C} = 0.038\ eV$, $\sigma_{Ni-C} = 2.84$ Å, $\varepsilon_{Cu-C} = 0.034\ eV$ and $\sigma_{Cu-C} = 2.86$ Å. For Ni–C and Cu–C interactions, a cutoff radius of 2.5σ Å were used.

The Lorentz-Berthelot rules have been successfully used to simulate the interaction between atoms of different solid surfaces (Fang and Wu, 2008; Li et al., 2016), but there is some controversy in its ability to adequately reflect the interactions among unlike atoms (Wang et al., 2010). The LB rules are shown to be unable to predict accurately the interactions of vapor-liquid mixtures (Delhommelle and Millié, 2001). However, it has been successfully used to depict the unlike fluid-solid interaction when methane is absorbed on graphite (Forte et al., 2014) or to study the adsorption process of methane/water vapor mixtures on porous activated carbons (Müller et al., 2000; Müller and Gubbins, 1998). Additionally, the Lorentz-Berthelot combining rule was selected to simulate the cross interactions between water, CO2, and silica atoms (Jiang et al., 2017). Furthermore, Leroy et al. (Leroy and Müller-Plathe, 2015) introduced the dry-surface methodology to determine the work of adhesion of solid–liquid interfaces. For this purpose, the interactions were obtained using the Lorentz–Berthelot mixing rules. Finally, Lorentz-Berthelot rules has been successfully used to simulate the interaction between atoms of different solid surfaces (Fang and Wu, 2008; Li et al., 2016).

The MD simulation involves a diamond spherical indenter that penetrates the surface of Ni and Cu samples in a cycle of loading and unloading. Fig. 1 a) shows the initial simulation arrangement where the bulk material and the indenter were initially separated by a sufficient distance to prevent them from interacting with each other before the indentation process. Ni and Cu substrates were divided into two different layers, i.e., Newtonian atoms and boundary atoms (Fig. 1 a). Initially, an energy minimization of the system was carried out at 0 K. This process allowed to adequately adjust the coordinates of the atoms in the space in which they were confined by means of the conjugate gradient algorithm, avoiding overlaps in the positions of the atoms.

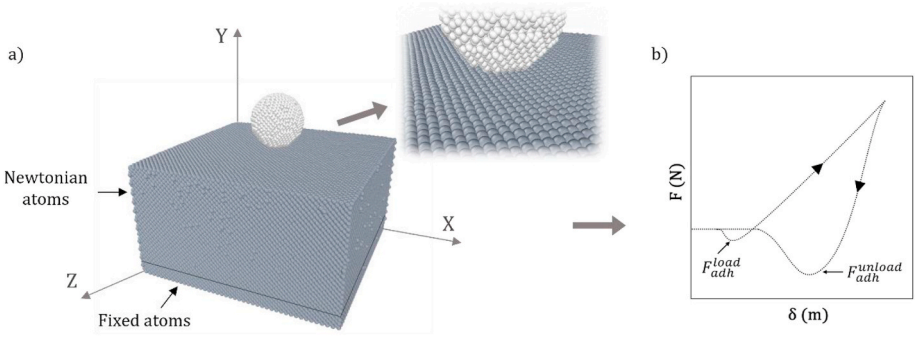

Fig. 1. a) MD model of the indentation with a spherical tip and b) theoretical curve of a spherical indentation test with adhesion.

Then, the MD model was set to 300 K assuming a canonical (NVT) ensemble with a Nose-Hoover thermoset for 60 ps. After this equilibrium procedure, the simulation process was carried out in a loading and unloading cycle under a micro-canonical (NVE) ensemble. The bottom layers of bulk atoms, with a total thickness of 5 Å in the Y direction, were fixed in their initial lattice positions during the simulation. Newtonian atoms in the upper atom layers were free to move and their equations of motion were integrated using the Verlet's velocity algorithm (Verlet, 1967). Periodic boundary conditions were applied in X and Z directions. The indenter was moved toward the sample surface along the Y direction at a constant velocity of 20 m/s until a maximum indentation depth of 11 Å was reached. After that, the indenter was moved away from the contact surface at the same velocity. The indentation velocity was selected following the recommendations reported in previous works (Alhafez et al., 2015; Fang et al., 2009; Fu et al., 2016; Goel et al., 2014; Hasnaoui et al., 2004; Yang et al., 2016).

In addition, indentations were carried out on Ni and Cu without taking into account adhesion effects. These simulations were done with the same procedure as the previous, but considering an infinitely stiff indenter, simulated with the "indent" command provided by LAMMPS. The spherical indenter exerts a force defining by $F = -K(r-R)^2$, where K is the proportionality force constant, R is the radius of the indenter and r is the distance between the Newtonian atoms and the indenter profile. In this case, the proportionality constant was chosen as 10 eV/Å and the indenter radius was 20 Å. For all simulations, the variation of the system temperature did not exceed 10 K during the indentation process.

Prior to the indentations analyses, MD simulations of tensile process on Ni and Cu were planned to follow a similar procedure to that described by Rassoulinejad-Mousavi et al. (2016). For these tensile simulations, a cubic box with size of 50 times the lattice parameter of each material was considered. Periodic boundary conditions were imposed in all directions other than the loading one. Tensile tests were carried out imposing a strain rate of 10^{-3} ps^{-1} in two crystal orientations: (100) and (111). The elastic constants on each orientation were determined and, from them, the Young's modulus for Ni and Cu. The values so calculated were used as a reference for those obtained from indentation.

2.2. Analysis procedure

The indentation modulus of Ni and Cu, and the adhesion energies of the Ni–C and Cu–C interactions were determined combining MD simulations with the Maugis-Dugdale contact model (Maugis, 1992). The Pietrement- Troyon (PT) approximation (Pietrement and Troyon, 2000) of the Maugis-Dugdale model was used, following the step-by-step procedure described in the next paragraphs.

Load-penetration depth data. Adhesion effects are relevant for the lowest penetration depths during the loading and unloading process. Fig. 1 b) shows a theoretical curve of a spherical indentation with adhesion effect, in which tensile forces are indicated (black arrows in Fig. 1 b), whose maximum values are used to determine the adhesion force. Two maximum tensile values can be identified, one on the loading curve, F_{adh}^{load} and one on the unloading curve, F_{adh}^{unload}.

Estimation of the effective radius. This is an essential point in the procedure and one of the contributions of this work.

During the indentation processes here analysed, a hysteresis effect appears in the loading-unloading cycle because of the permanent deformation experienced by the indented material. Therefore, the radius of the residual imprint in the substrate affects the unloading branch analysis, which is the one that is actually used in the analysis under the hypothesis commonly used in indentation tests that the reloading would return to being elastic.

The proposal used in this work to obtain the effective radius in the unloading branch is based on the following hypotheses.

- The adhesion force is a function exclusively of the effective radius and of the adhesion energy which is a constant of the system (this is the case in the DMT and JKR models and it is assumed that it is also the case in the transition described by the Maugis theory).
- The first adhesion force that is registered in the loading branch is produced at very small levels of force that would guarantee an elastic deformation regime, therefore the effective radius coinciding with the radius of the indenter.

Equations (A.6) and (A.9) provide the adhesion force expressions for the JKR and DMT models, respectively. Both equations establish a relationship between the force and the energy of adhesion through the effective radius of indentation, and differ only in one constant, 3/2 for the JKR model and 2 for the DMT model. It can be inferred that for any adhesion model, between JKR and DMT, a similar equation can be formulated, where the difference is the constant that affects the adhesion energy and the effective indentation radius. If the adhesion energy ω is considered as constant, adhesion forces are proportional to the effective radii in each branch of the indentation process. For very low penetration depths in the loading branch, where the initial adhesion between the bulk and indenter atoms is relevant, it is assumed that the behaviour can be considered linear elastic and the adhesion force F_{adh}^{load} is proportional to the radius of the indenter R_i. But, in the unloading branch, preceded by permanent deformation, F_{adh}^{unload} is proportional to the effective radius R^*. Equating the expressions for the adhesion energy in the loading and unloading branch, the effective radius R^* can be determined as:

$$R^* = \frac{F_{adh}^{unload}}{F_{adh}^{load}} R_i \tag{6}$$

Development of the PT approximation of the Maugis-Dugdale model. In equations (A.15), (A.16) and (A.17) of the Maugis-Dugdale model, the contact radius, a, the force, F, and the displacement, δ, depend on the adhesion energy, ω and on the combined modulus, E^*. These last two properties are the ones to be determined from an indentation test;

therefore, they are initially unknown. Because of that, a new parameter, χ, was defined as the ratio between ω and E^*:

$$\chi = \frac{\omega}{E^*} \tag{7}$$

This parameter allows you to rewrite equations (A.10), (A.15), (A.16) and (A.17), expressing the Tabor parameter μ and the normalised values of contact radius $\overline{a}$, force $\overline{F}$ and displacement $\overline{\delta}$ as follows:

$$\mu = \left(\frac{R^*\chi^2}{z_0^2}\right)^{\frac{1}{3}} \tag{8}$$

$$\overline{a} = a\left(\frac{4}{3\pi\chi R^{*2}}\right)^{\frac{1}{3}} \tag{9}$$

$$\overline{F} = \frac{F}{\pi\chi E^* R^*} \tag{10}$$

$$\overline{\delta} = \delta\left(\frac{16}{9\pi^2\chi^2 R^*}\right)^{\frac{1}{3}} \tag{11}$$

Iterative procedure to determine the Young's modulus and adhesion energy. Both properties were obtained from an iterative algorithm, trying to reproduce, through the Maugis-Dugdale model, the unloading branch obtained from MD simulations. The iteration begins by assigning a value of 0.01 for the transition parameter λ ($\lambda = 1.16\mu$) introduced by Maugis (1992). By using equations (A.11) and (A.19), the Tabor parameter μ and the nondimensional parameter α used in the PT approximation are calculated, respectively. Equation (8) can be used to determine the χ parameter by using the value of the effective radius R^* given by eq. (6) and the distance z_0 from the LJ potential. Then, the functions $S_{(\alpha)}$, $\beta_{(\alpha)}$, $\overline{F}_{adh}$ and $\overline{a}_{0(\alpha)}$ are determined from equations (A.20), (A.21), (A.22) and (A.23), respectively. The contact radius at zero indentation force, $a_{0(\alpha)}$, calculated from equation (9) and the adhesion force, F_{adh}, from the unloading MD simulated curve, are substituted into equation (A.17) for finally obtain the displacement δ corresponding to each value of the force during the unloading cycle. Following this procedure, the unloading curve predicted by the Maugis-Dugdale model can be drawn for each value of the parameter λ. Each curve was compared with that obtained from the MD simulations and the relative difference in displacement at each point on the curve was evaluated. The root mean square error (RMSE) was used to evaluate the discrepancy between the curves simulated by molecular dynamics (MD) and those predicted by the PT approximation (PT):

$$E_{RMS} = \sqrt{\frac{1}{N}\sum_{i=1}^{N}(\delta_{MD} - \delta_{PT})^2} \tag{12}$$

where the displacement difference, $\delta_{MD} - \delta_{PT}$, was evaluated for each point of the unloading curve; and N is the number of data points. The curve that gave the minimum value of the ERMS was used to determine the optimal values of the parameters λ, α, and μ. The best estimate of the adhesion energy ω can be obtained with F_{adh} and equations (A.16) and (A.23). The optimal parameter χ can be found with equation (8) and, finally, the effective modulus of elasticity E^* is obtained from equation (7). The algorithm described has been outlined in the flowchart of Fig. 2.

3. Results

This section begins by presenting the values of the elastic constants obtained from MD simulations of tensile tests. These simulations allowed to validate the Cu and Ni potentials that were then used in the indentation. Subsequently, the indentation force-displacement curves obtained from MD simulations are presented. Finally, a reliable contact model is applied to the indentation data and Young's modulus and adhesion energies are determined.

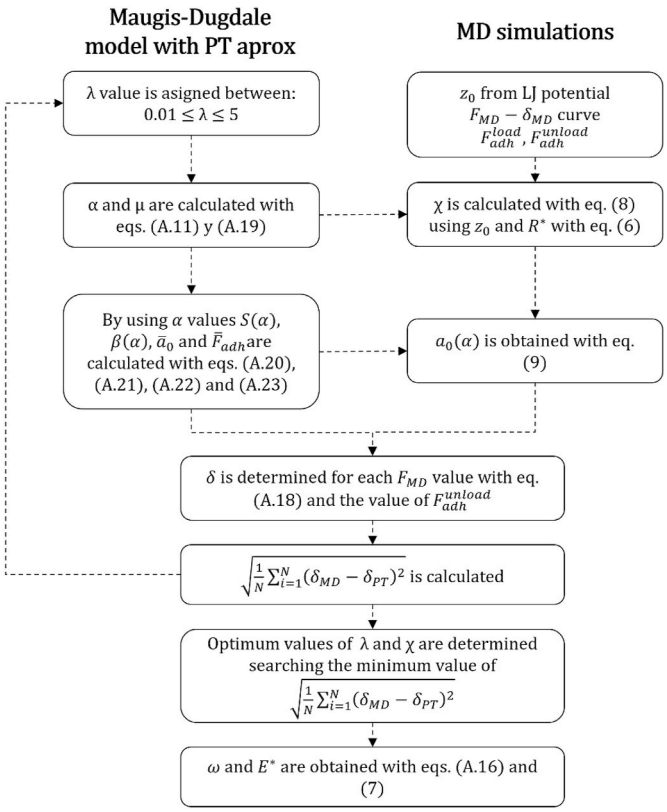

Fig. 2. Flow chart describing the algorithm followed to obtain adhesion energy and elastic modulus.

3.1. Assessment of the MD model used by simulations of a tensile test

To validate Ni and Cu potentials selected in the MD model, simulations of a uniaxial tensile test were carried out. Table 1 shows the values of the elastic constants C_{11}, C_{12} and C_{44} for Cu and Ni, provided by the simulations, as well as the corresponding values of the Young's modulus, E, and Poisson's ratio, ν, derived from these constants. As can be seen, the value of the elastic constant C_{11} was higher when the crystallographic orientation varies from (100) to (111). However, constants C_{12} and C_{44} showed the opposite tendency. This behaviour has been observed for both materials and the obtained values show a high agreement with those reported by Rassoulinejad-Mousavi et al. (2016).

Ledbetter (1981) determined the elastic constants of polycrystalline Cu between 4 and 295 K by measuring the longitudinal and transverse ultrasonic velocities. Five elastic constants were measured: longitudinal modulus, shear modulus, Young's modulus, bulk modulus, and Poisson's ratio. He reported a value of 128.17 GPa for the Young's modulus and 0.3471 for the Poisson ratio at 295 K. These values are very similar to those obtained in our work (Table 1). Kimura (1933) determined the values of the second-order adiabatic elastic stiffnesses constant for single crystal of Cu at room temperature. He reported values of 173.3 GPa, 118.2 GPa and 61.2 GPa for the elastic constants C_{11}, C_{12}, and C_{44}, respectively. Additionally, Jacobsen (1954), reported the following values for the elastic constants of the Cu at room temperature: $C_{11} = 170$

Table 1
Elastic constants of Cu and Ni obtained from MD simulations of tensile tests.

Material	C_{11} (GPa)	C_{12} (GPa)	C_{44} (GPa)	E (GPa)	ν
Copper <100>	150	110	71	115	0.34
Copper <111>	189	91	52	134	0.32
Nickel <100>	214	141	121	195	0.30
Nickel <111>	287	108	93	232	0.27

GPa, $C_{12} = 124$ GPa and $C_{44} = 64.5$ GPa. Comparing all these values to those shown in Table 1, a significant similarity can be observed.

Neighbours et al. (Neighbours, J et al., 1951) determined the elastic constants of Ni by the pulsed ultrasonic method. In that work, wave velocity measurements on four Ni single crystals of general orientation that were magnetically saturated were combined by the approximation method leading to values of the elastic constants $C_{11} = 253$ GPa, $C_{12} = 152$ GPa and $C_{44} = 124$ GPa. Raman et al. (Raman and Krishnamurti, 1955) evaluated the mean values of the elastic constants of single crystals of Ni determined by ultrasonic pulse method at room temperature. The values reported were $C_{11} = 252.6$ GPa, $C_{12} = 155.1$ GPa and $C_{44} = 123$ GPa. These values are similar to those shown in Table 1.

Consequently, the selected EAM potentials provided reliable values for the elastic constants of Ni and Cu.

3.2. Simulations of the indentation process

Before starting to show simulation results about the indentation process, it must be taken into account that at these small scales the anisotropy of the material can have an effect that has not been considered in this work. An analysis that combines adhesion and anisotropy is extremely complex. The hypothesis of this work was that the properties measured by indentation can be considered as weighted averages that can be compared with the elastic modulus of the bulk material.

Fig. 3 shows different moments during the indentation: the instant when the indenter approaches the metal surface during the loading cycle can be observed in Fig. 3 a) and 3 e) for Cu and Ni, respectively; the point in the loading cycle when the force is maximum in Fig. 3 b) and 3 f), for Cu and Ni, respectively; permanent deformation and pile up that occurs after indentation are shown in Fig. 3 c) and 3 g) for Cu and Ni, respectively; and residual indentation imprint for Cu and Ni in Fig. 3 d) and 3 h), respectively. Additionally, the spherical shape and radius of the indenter was preserved during the indentation process.

Fig. 3 i) shows representative force-displacement curves obtained from MD simulations of the indentation process on Cu and Ni. These curves were formed by a loading and unloading branch. Continuous fluctuations were observed in both, being more pronounced during loading. Also, the greater the depth of penetration of the loading process, the more pronounced they are.

At very shallow penetration depths for both cycles, the load showed negative values (points a, c, e and g in Fig. 3 i), signifying tensile forces because of an evident adhesion effect.

To verify the influence of the displacement rate and, therefore, the reliability of the force-displacement data, simulations of the indentation process at different velocities were carried out. Fig. 4 compares the indentation force-displacement curves at different velocities: 20 m/s, 10 m/s, 5 m/s and 2 m/s. All the curves mostly overlap, both in the loading and unloading cycles. Thus, Fig. 4 showed that the velocity did not have a significant effect on the indentation process, at least for the values analysed (between 2 and 20 m/s). Similar results have been previously reported by other researchers. Nair et al. (2009) carried out atomistic simulations of nanoindentation tests on a 20-nm-thick Ni thin film oriented in the [111] direction to study the effects of indenter velocity and radii, interatomic potentials, and the boundary conditions used to represent the substrate. The simulation results were compared directly with experimental results of Ni thin film of the same thickness and orientation. In that work, two indenter velocities were chosen: 10 m/s and 2.5 m/s. They found that these velocities had no significant effect on either the elastic region or the hardness values of the film obtained from the simulations. Therefore, our analysis was carried out from here on,

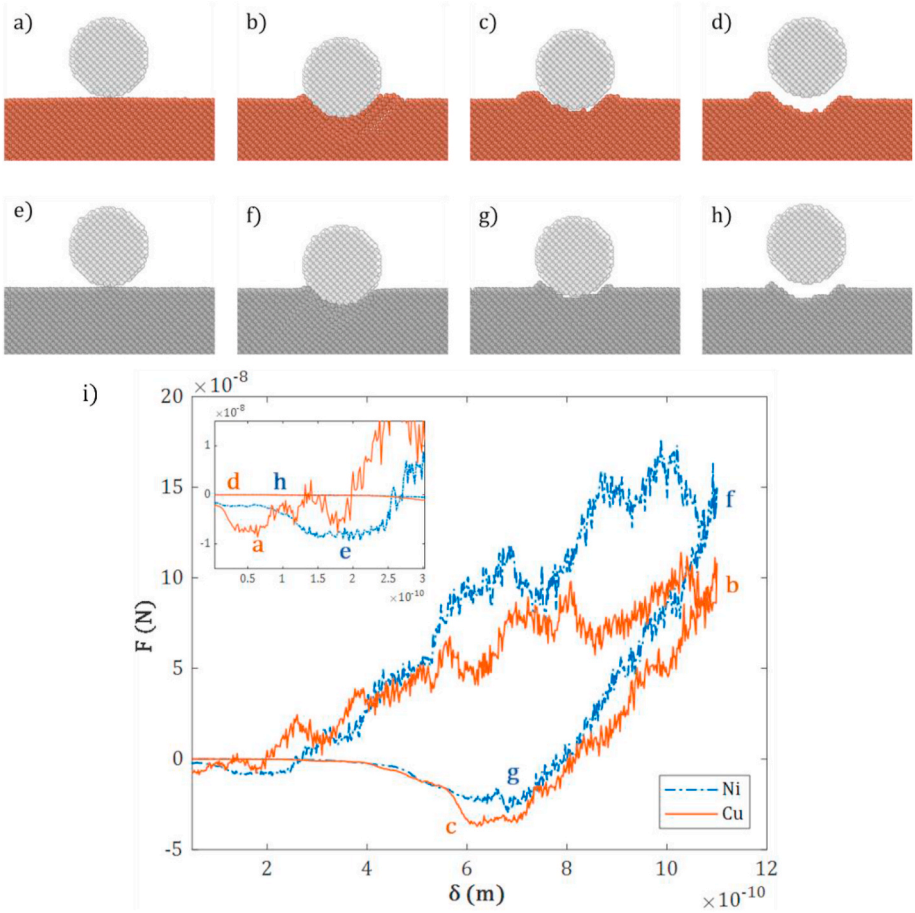

Fig. 3. A detail of different moments in a typical MD summation of the indentation process onto Cu (a, b, c and d) and Ni (e, f, g and h).

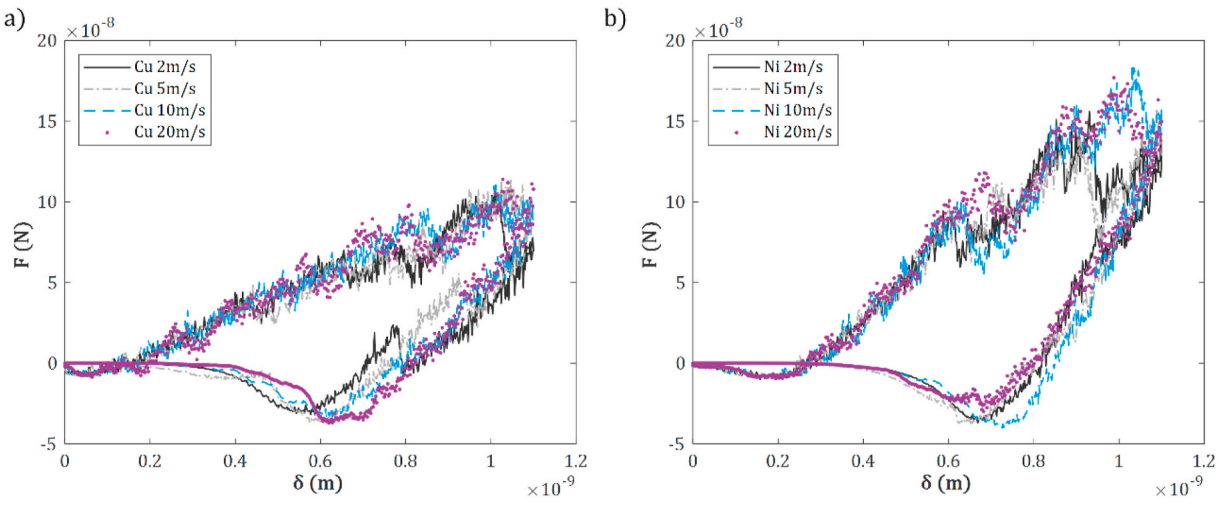

Fig. 4. Force-displacement indentation curves simulated at different velocities: a) comparison for Cu; b) comparison for Ni.

only for the indentation curves at 20 m/s. Additionally, Fu et al. (2016) performed molecular dynamics simulation of nanoindentation on Cu/Ni nanotwinned multilayer films using a spherical indenter. Simulations of the indentation process at different velocities were reported. They observed that the P-h curves corresponding to different indentation speeds for Cu or Ni were very close to each other, indicating that the effects of the speed range from 1 to 50 m/s were not significant.

3.3. Maugis-Dugdale model

Fig. 5a) shows the unloading curve during Cu indentation, comparing the result of a MD simulation with the predictions of the Maugis-Dugdale model (PT approximation), once optimized according to the iterative procedure described in 2.2 (Fig. 2). The optimal value of the λ parameter was 0.26, resulting in an adhesion energy value of 0.75 J/m^2. The effective modulus of elasticity was 114 GPa and the nominal modulus, considering a Poisson's ratio of 0.34 (Table 1), was 129 GPa.

Fig. 5 b) shows the unloading Ni indentation case, comparing again the MD simulated curve with that predicted by the Maugis-Dugdale model. The iterative procedure provides an optimal value of the parameter λ of 0.17. The corresponding adhesion energy was 0.80 J/m^2, the effective elastic modulus was 198 GPa and the nominal modulus was 217 GPa, selecting a value of 0.3for the Poisson's ratio (Table 1). It should be noted that although only the unloading curve is represented in the above analyses, the loading branch has been used to determine F_{adh}^{load} and the effective radius.

4. Discussion

This section highlights the suitability of models based on continuum mechanics. A combination of MD simulations together with the application of the Maugis-Dugdale adhesion model has been used to determine the elastic modulus and adhesion energy of Cu and Ni from indentation with a spherical diamond tip.

Fig. 6 a) shows the force-displacement curves during unloading in a nanoindentation test on Cu. The comparison includes the curves provided by the MD simulation with and without adhesion (INDENT command in LAMMPS). The maximum force reaches 100 nN and neglecting the adhesion zone is inadmissible in this material at this scale, since the magnitude of the adhesive forces reaches an absolute value of 40% of the maximum force applied. In the case of Ni, shown in Fig. 6 b), the maximum forces exceed 150 nN and adhesion forces are similar, in this case these forces are approximately 30% of force applied. In any case, the curve allows the adhesion energy to be determined through the iterative process of the Maugis-Dugdale model, as indicated in section 2.2.

Several attempts to experimentally measure the adhesion energy on an atomic scale between graphene and Cu or Ni have been reported. For

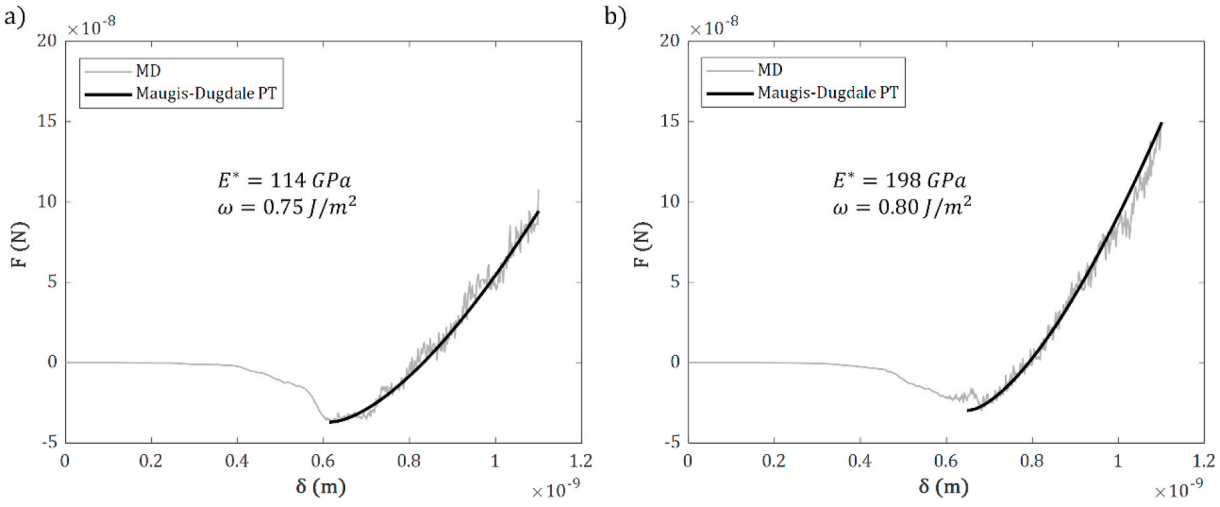

Fig. 5. Comparison between MD simulated unloading curve and the Maugis-Dugdale prediction: a) for copper; b) for nickel.

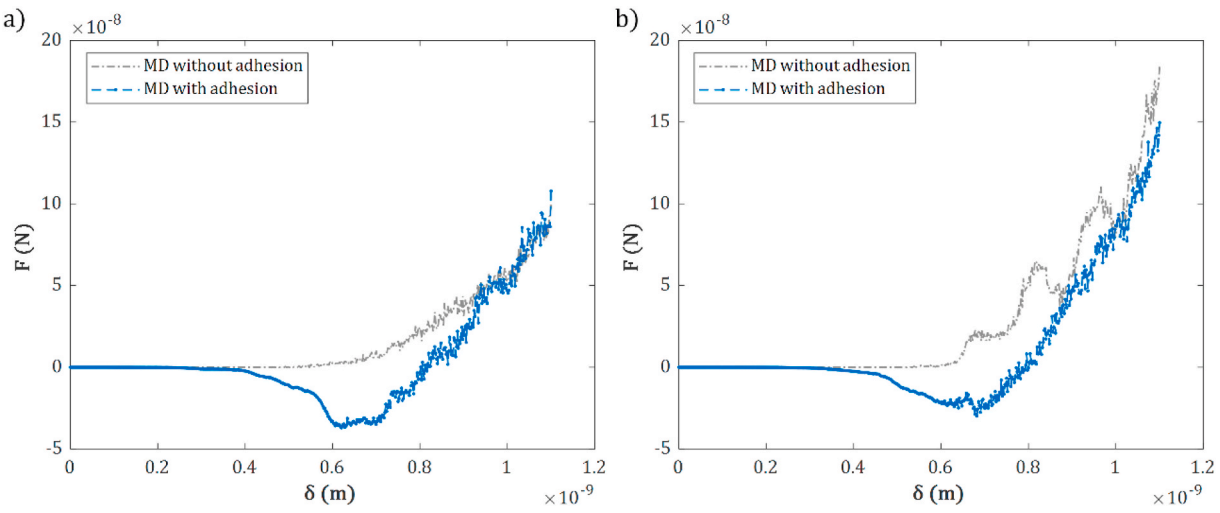

Fig. 6. Force-displacement curves during unloading in a nanoindentation test: comparison between MD simulation with and without adhesion: a) Cu; b) Ni.

example, Jiang et al. (Jiang and Zhu, 2015) presented a new method to measure adhesion between graphene and different materials using AFM with a microsphere tip. They measured the adhesion energy of monolayer graphene to Cu, reporting a value of 0.75 J/m^2, just the very same value. Similarly, Yoon et al. (2012) determined the adhesion of monolayer graphene on Cu by double cantilever beam tests. They reported a value for the adhesion energy of 0.72 J/m^2. Even though these two reported values are so close, a large discrepancy has generally been observed when comparing experimental values of adhesion energy. This circumstance was pointed out by Chang et al. (2019) where differences of up to an order of magnitude have been reported.

To determine the adhesion energy from the indentation force-displacement curve, it is necessary to have a criterion that indicates the most suitable contact model for each case. If it is decided to simply use a JKR or DMT model, errors of up to 25% can be made, since these are the differences between the expressions that relate the adhesion forces and the adhesion energy in both models (equations A.6 and A.9). The Maugis-Dugdale model describes a continuous transition between the DMT and JKR contact models as the λ parameter increases. Fig. 7a) represents the normalised adhesion force versus λ, showing two asymptotes, one at low values of λ (DMT model) and another at high values of λ (JKR model). The points corresponding to the contacts analysed in this work are also represented in Fig. 7a). Ni–C and Cu–C are found in the intermediate transition zone between both models. Consequently, for both cases, the estimation of the adhesion energy by the JKR or DMT models might not be appropriate. Fig. 7a) provides information on the relationship between force and adhesion energy. However, in an indentation test it is also convenient to evaluate the importance of the adhesion in terms of the global scale of the test, which will be characterised by the value of the maximum indentation force. Fig. 7b) shows an adhesion map in which the total force applied during indentation, normalised with the adhesion energy, is plotted against λ parameter (implicitly dependent on the effective radius).

This map (M. Ciavarella et al., 2019a) allows us to get an idea of the relative importance of adhesion effects. When the maximum forces in the test are high with respect to the adhesion energy, the Hertz model is a good approximation. In the map of Figure b) below the Hertz limit are the Bradley contact models (Bradley, 1932) for rigid solids, and the DMT, Maugis-Dugdale and JKR models for deformable materials. The parameter λ evaluates the relative importance of the forces of adhesion in relation to elastic forces. The further to the right we place the greater the relative importance of the adhesion forces in relation to the elastic ones. As can be seen in Fig. 7 b), Ni–C and Cu–C are clearly in intermediate region that only the Maugis-Dugdale correctly describes. This means that neither the Hertz approximation nor that of the DMT and

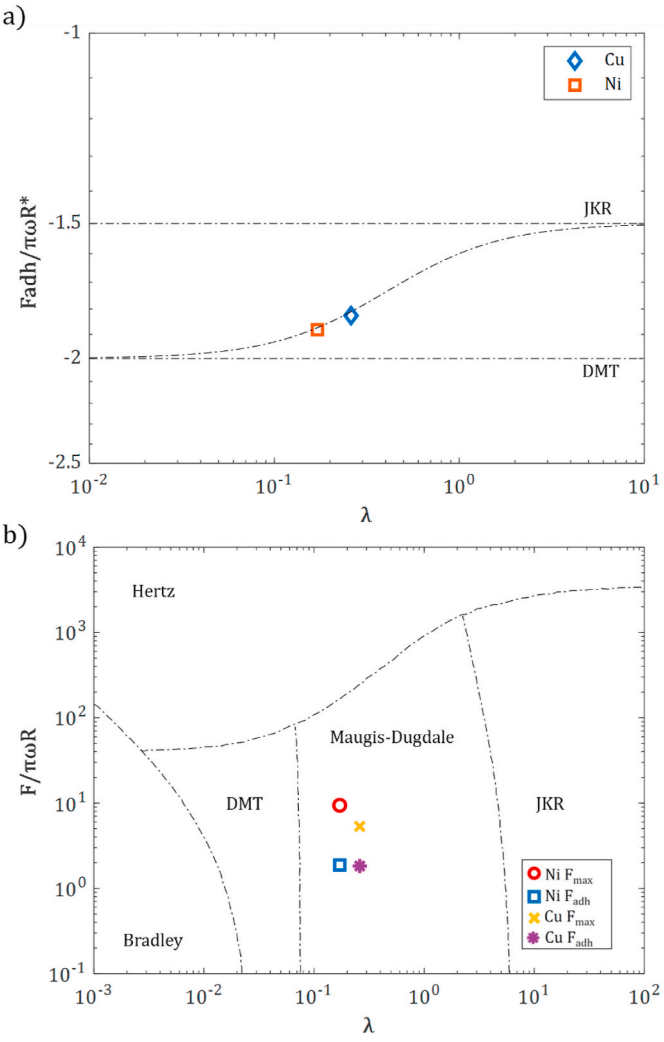

Fig. 7. *a) Normalised adhesion force versus λ parameter (dashed-dotted lines from (Maugis, 1992)). b) A contact model map: normalised indentation force versus λ parameter (dashed-dotted lines from (Johnson and Greenwood, 1997)).*

JKR models will give consistent results. The values of the normalised force must be much higher, almost two orders of magnitude in a first estimate, for the Hertz approximation to be fully useable in the case of Ni and Cu at this small scale.

One last consideration to keep in mind. All the previous analysis has been based on the assumptions that the interaction between tip and substrate is dominated by Van der Waals forces and, consequently, the choice of an LJ-type potential is appropriate (Dong et al., 2013). Therefore, the analysis does not consider those problems where friction is very relevant.

5. Conclusions

In this work, a very low-scale indentation test between a spherical diamond tip and plane Cu and Ni samples has been studied by combining MD simulations and continuum mechanics-based models. An algorithm founded on the Maugis-Dugdale theory with the Pietrement-Troyon approximation has been developed which, from the force-displacement curves of the complete loading and unloading cycle, allows the adhesion energy and the elastic modulus to be determined simultaneously.

The developed procedure takes into account the presence of inelastic deformations by determining the effective radius, from the radius of the indenter and the residual imprint after the test.

This work evidences the importance of adhesion effects in Ni and Cu nanocontacts. The correct identification of the model to describe the contact between two materials, allows a correct estimation of the adhesion energy and the mechanical properties through indentation tests in a sphere-plane configuration. The selection of the Maugis-Dugdale model for the Ni–C contact and the Cu–C contact has made it possible to determine reliable values of adhesion energies for both systems, obtaining values of 0.80 J/m^2 and 0.75 J/m^2, respectively. Other models commonly used in the literature (Hertz, JKR and DMT) do not provide consistent results at these small scales.

Author's statement

S. Gonzalez-Tortuero: Conceptualization, Methodology, Investigation. Writing – original draft. **M.A. Garrido**: Conceptualization, Methodology, Investigation, Formal analysis, Writing – review & editing. **J. Rodríguez**: Conceptualization, Methodology, Formal analysis, Writing – review & editing, Funding acquisition.

Declaration of competing interest

The authors declare that they have no known competing financial interests or personal relationships that could have appeared to influence the work reported in this paper.

Data availability

Data will be made available on request.

Appendix. Equations for adhesion contact models

For an elastic surface compressed by an elastic spherical indenter, the classical Hertzian contact theory, based on the small strain assumption, gives the following relationships for the contact displacement, δ_H, the contact radius, a_H, and the indentation load, F (Johnson, 1985):

$$\delta_H = \frac{a_H^2}{R^*} \tag{A.1}$$

$$a_H = \left(\frac{FR^*}{K}\right)^{\frac{1}{3}} \tag{A.2}$$

where K is the elastic constant given by $K = \frac{4}{3}E^*$. In this expression, $E^* = \left[\frac{(1-\nu^2)}{E} + \frac{(1-\nu_i^2)}{E_i}\right]^{-1}$ and $R^* = \left[\frac{1}{R_i} - \frac{1}{R}\right]^{-1}$ are known as the effective elastic modulus and the effective radius, respectively. E_i and E are the elastic moduli, ν_i and ν are the Poisson's ratios, of the indenter and the surface, respectively. Additionally, R_i and R are the radius of curvature of the indenter and the residual impression of the surface (Fischer-Cripps, 2011). Obviously, for an elastic indentation, the curvature radius of the surface is infinite, so the effective radius is equal to the indenter one.

In a typical nanoindentation experiment, the force and displacement of the indenter are continuously recorded during a cycle of loading and unloading. If permanent deformation occurs during the loading process, a residual imprint is left on the indented surface when the load is removed. During the unloading process, the material tries to recover its original shape and the final curvature is a consequence of unrecoverable deformations inside the material. Consequently, equations (A.1) and (A.2) can be used during unloading taking the residual indentation radius, R_r, as the surface radius.

As described in the introduction section, when nanoindentation tests are scale down to the nanoscale, adhesion effects can contribute significantly. Therefore, equations (A.1) and (A.2) must be modified to take them into account. These effects are controlled by the atomic interaction between the surfaces in contact, E_{LJ}, which can be described by a Lennard-Jones potential (Lennard-Jones, 1931) as shown below:

$$E_{LJ}(r) = 4\varepsilon\left[\left(\frac{\sigma}{r}\right)^{12} - \left(\frac{\sigma}{r}\right)^{6}\right] \tag{A.3}$$

where r is the distance between atoms and ε and σ are the potential parameters that establish the energy and separation distance scales, respectively. The depth of the well is represented by ε and σ is the distance at which the interaction between two particles is equal to zero.

For a spherical adhesive contact, there are two well-known analytical models in the literature. Johnson, Kendall and Roberts (Johnson et al., 1971) presented a theory for spherical contact assuming that the adhesive forces occur entirely within the contact area. The JKR model is described by equations (A.4) and (A.5):

$$\delta_{JKR} = \frac{a^2}{R^*} - \frac{4}{3}\sqrt{\frac{aF_{adh}}{R^*K}} \tag{A.4}$$

$$a_{JKR} = \left[\frac{R^*}{K}\left(\sqrt{F_{adh}} + \sqrt{F + F_{adh}}\right)^2\right]^{\frac{1}{3}} \tag{A.5}$$

where F_{adh} represents the maximum force of adhesion and is defined as the force necessary to separate the two surfaces in contact. This force depends on the energy adhesion, ω, between the indenter and the surface. The JKR model predicts the following relationship for the adhesion force:

$$F_{adh} = -\frac{3}{2}\pi\omega R^* \tag{A.6}$$

Derjaguin, Muller and Toporov (Derjaguin et al., 1975) proposed a model of adhesive spherical contact, in which the surface forces do not modify the deformed profile of the sphere predicted by Hertz. The attractive forces only exist outside the contact area and are balanced by the compression force within it. According to DMT model, displacement and contact radius are given by equations (A.7) and (A.8):

$$\delta_{DMT} = \frac{a^2}{R^*} \tag{A.7}$$

$$a_{DMT} = \left[\frac{R^*}{K}(F + F_{adh})\right]^{\frac{1}{3}} \tag{A.8}$$

and the adhesion force is given by equation (A.9):

$$F_{adh} = -2\pi\omega R^* \tag{A.9}$$

The above continuum mechanics-based models are strictly suitable only for two limiting cases, i.e., the JKR model is valid for a large soft sphere and the DMT model is valid for a small rigid sphere. For intermediate cases, Tabor (1977) proposed a parameter μ that allows to characterize the adhesive contact. This dimensionless parameter is given by equation (A.10):

$$\mu = \left(\frac{R^*\omega^2}{E^{*2}z_0^2}\right)^{\frac{1}{3}} \tag{A.10}$$

where z_0 is the equilibrium distance in the LJ potential (Michele Ciavarella et al., 2019b). For high values of the Tabor parameter, the JKR model correctly describes the adhesion, while for low values, the DMT model better fits the adhesive behaviour.

A complete transition between the JKR and DMT models is captured through a more generalized adhesive contact theory between an arbitrary shaped axisymmetric rigid punch and an elastic half-space proposed by Maugis (1992). According to this model, the intimate contact occurs in a circular region of radius a, but the interaction extents over a larger circular region of radius c. This theory is known as Maugis-Dugdale model and it introduced another dimensionless parameter, similar to that of Tabor, called the transition parameter, λ, as indicated in equation (A.11):

$$\lambda = 2\sigma_0\left(\frac{R^*}{\pi K^2\omega}\right)^{\frac{1}{3}} \quad (\lambda = 1.16\mu) \tag{A.11}$$

where σ_0 is the maximum attractive force in the Lennard–Jones potential. It is assumed that σ_0 exerts an influence over an area of radius c that is greater than the actual contact radius a. The Maugis parameter is related to Tabor's by $\lambda = 1.16\mu$. This relation was obtained by Johnson and Greenwood (1997) assuming a Dugdale force-separation law between the surfaces in contact.

The JKR theory is applicable to those cases where $\lambda > 5$ and the DMT model in those others where $\lambda < 0.1$. Both models are two particular cases of the more general Maugis-Dugdale theory. As λ increases from zero to infinity, there is a continuous transition from the DMT to the JKR approximation. The Maugis equations are:

$$\frac{\lambda\overline{a}^2}{2}\left[\left(m^2-2\right)tan^{-1}\left(\sqrt{m^2-1}\right) + \left(m^2-1\right)\right] +$$

$$\frac{4\lambda^2\overline{a}}{3}\left[\sqrt{m^2-1}\,tan^{-1}\left(\sqrt{m^2-1}\right) - m + 1\right] = 1 \tag{A.12}$$

$$\overline{F} = \overline{a}^3 - \lambda\overline{a}^2\left(\sqrt{m^2-1} + m^2\tan^{-1}\sqrt{m^2-1}\right) \tag{A.13}$$

$$\overline{\delta} = \overline{a}^2 - \frac{4\lambda\overline{a}}{3}\sqrt{m^2-1} \tag{A.14}$$

where the m parameter is given by the ratio c/a and $\overline{a}$, $\overline{F}$ and $\overline{\delta}$ are the normalised values of the contact radius, the normal force, and the indentation depth, respectively. They are defined by the following equations:

$$\overline{a} = a\left(\frac{K}{\pi\omega R^{*2}}\right)^{\frac{1}{3}} \tag{A.15}$$

$$\overline{F} = \frac{F}{\pi\omega R^*} \tag{A.16}$$

$$\overline{\delta} = \delta\left(\frac{K^2}{\pi^2\omega^2 R^*}\right)^{\frac{1}{3}} \tag{A.17}$$

However, if the adhesion energy, ω, is unknown, the solution proposed by Maugis-Dugdale model is complex and tedious because an intricate iterative procedure has to be used. To partially overcome this difficulty, empirical approximations of the Maugis-Dugdale model have been developed [49, 50]. The empirical approximation proposed by Pietrement and Troyon (PT) simplifies the relationship between the indentation depth and the external force according to equation (A.18):

$$\delta = \frac{a_{0(\alpha)}^2}{R}\left[\left(\frac{\alpha+\sqrt{1+\frac{F}{F_{adh}}}}{1+\alpha}\right)^{\frac{4}{3}} - S_{(\alpha)}\left(\frac{\alpha+\sqrt{1+\frac{F}{F_{adh}}}}{1+\alpha}\right)^{\frac{2\beta_{(\alpha)}}{3}}\right] \tag{A.18}$$

where $a_{0(\alpha)}$ is the contact radius at zero indentation force and α is a nondimensional parameter. PT approximation proposes the following relationship between α and λ given by:

$$\lambda = -0.913\ln(1-1.018\alpha) \tag{A.19}$$

In equation (A.18), $S_{(\alpha)}$ and $\beta_{(\alpha)}$ are also functions of α given by:

$$S_{(\alpha)} = -2.160\alpha^{0.019} + 2.7531\alpha^{0.064} + 0.073\alpha^{1.919} \tag{A.20}$$

$$\beta_{(\alpha)} = 0.516\alpha^4 - 0.683\alpha^3 + 0.235\alpha^2 + 0.429 \tag{A.21}$$

Similarly, the nondimensional parameters of equations (A.15) and (A.16) can be also expressed in terms of α:

$$\overline{a}_{0(\alpha)} = -0.451\alpha^4 + 1.417\alpha^3 - 1.365\alpha^2 + 0.950\alpha - 1.26 \tag{A.22}$$

$$\overline{F}_{ad} = 0.267\alpha^2 - 0.767\alpha + 2.00 \tag{A.23}$$

Pietrement and Troyon [50] compared the indentation force-displacement curves for the Maugis-Dugdale model with those obtained from equation (A.18) for several values of λ, including the JKR and DMT solutions. They reported an accuracy less than 1%. The merit of the PT approach is to simplify the utilization of the Maugis-Dugdale equations and thus facilitate comparison with the different adhesion models in the literature. Therefore, given a value of the Maugis parameter, λ, the PT approximation, following equations (A.18) to (A.23), is revealed as a viable way to provide force and penetration depth data of indentation processes affected by adhesion.

References

Alhafez, I.A., Ruestes, C.J., Gao, Y., Urbassek, H.M., 2015. Nanoindentation of hcp metals: a comparative simulation study of the evolution of dislocation networks. Nanotechnology 27, 045706. https://doi.org/10.1088/0957-4484/27/4/045706.

Berthelot, D., 1898. Sur le mélange des gaz. C. R. Hebd. Seances Acad. Sci. 126, 1703–1855.

Bhushan, B., 2003. Adhesion and stiction: mechanisms, measurement techniques, and methods for reduction. J. Vac. Sci. Technol. B Microelectron. Nanom. Struct. 21, 2262–2296. https://doi.org/10.1116/1.1627336.

Bhushan, B., 2007. Nanotribology and nanomechanics of MEMS/NEMS and BioMEMS/BioNEMS materials and devices. Microelectron. Eng. 84, 387–412. https://doi.org/10.1016/j.mee.2006.10.059.

Bhushan, B., 2008. Nanotribology, nanomechanics and nanomaterials characterization. Philos. Trans. R. Soc. A 366, 1351–1381. https://doi.org/10.1098/rsta.2007.2163.

Bigl, S., Schöberl, T., Wurster, S., Cordill, M.J., Kiener, D., 2016. Correlative microstructure and topography informed nanoindentation of copper films. Surf. Coat. Technol. 308, 404–413. https://doi.org/10.1016/j.surfcoat.2016.07.104.

Birleanu, C., Pustan, M., Müller, R., Dudescu, C., Merie, V., Voicu, R., Baracu, A., 2016. Experimental investigation by atomic force microscopy on mechanical and tribological properties of thin films. Int. J. Mater. Res. 107, 429–438. https://doi.org/10.3139/146.111358.

Borodich, F.M., Galanov, B.A., 2008. Non-direct estimations of adhesive and elastic properties of materials by depth-sensing indentation. Proc. R. Soc. A Math. Phys. Eng. Sci. 464, 2759–2776. https://doi.org/10.1098/rspa.2008.0044.

Bradley, R.S., 1932. The cohesive force between solid surfaces and the surface energy of solids. Philos. Mag. J. Sci. 13, 853–862. https://doi.org/10.1080/14786449209461990.

Buchs, R., Basu, S., Elshrief, O.A., Coward, R., Barsoum, M., 2009. Spherical nanoindentation and Vickers microhardness study of the deformation of poled BaTiO3 single crystals. J. Appl. Phys. 105, 093540 https://doi.org/10.1063/1.3117496.

Cao, Z.H., Lu, H.M., Meng, X.K., 2009. Barrier layer and annealing temperature dependent microstructure evolution of nanocrystalline Cu films. Mater. Chem. Phys. 117, 321–325. https://doi.org/10.1016/j.matchemphys.2009.06.018.

Chandross, M., Lorenz, C.D., Stevens, M.J., Grest, G.S., 2008. Simulations of nanotribology with realistic probe tip models. Langmuir 24, 1240–1246. https://doi.org/10.1021/la702323y.

Chang, W., Rajan, S., Peng, B., Ren, C., Sutton, M., Li, C., 2019. Adhesion energy of as-grown graphene on nickel substrates via StereoDIC-based blister experiments. Carbon N. Y. 153, 699–706. https://doi.org/10.1016/j.carbon.2019.07.051.

Chasiotis, I., Bateson, C., Timpano, K., Mccarty, A.S., Barker, N.S., Stanec, J.R., 2007. Strain rate effects on the mechanical behavior of nanocrystalline Au films. Thin Solid Films 515, 3183–3189. https://doi.org/10.1016/j.tsf.2006.01.033.

Che, J., Cagin, T., Goddard, W.A., 1998. Generalized extended empirical bond-order dependent force fields including nonbond interactions. Theor. Chem. Acc. 102, 346–354. https://doi.org/10.1007/s002140050506.

Chen, R., 2020. Understanding Contact at the Nanoscale Using Molecular Dynamics Simulations. University of California, Merced.

Ciavarella, M., Joe, J., Papangelo, A., Barber, J.R., 2019a. The role of adhesion in contact mechanics. J. R. Soc. Interface 16. https://doi.org/10.1098/rsif.2018.0738.

Dai, L., Sorkin, V., Zhang, Y.-W., 2016. Effect of surface chemistry on the mechanisms and governing laws of friction and wear. Appl. Mater. Interfaces 8, 8765–8772. https://doi.org/10.1021/acsami.5b10232.

Ciavarella, M., Xu, Y., Jackson, R.L., 2019b. The generalized Tabor parameter for adhesive rough contacts near complete contact. J. Mech. Phys. Solid. 122, 126–140. https://doi.org/10.1016/j.jmps.2018.08.011.

Dai, Z., Lu, N., Liechti, K.M., Huang, R., 2020. Mechanics at the interfaces of 2D materials : challenges and opportunities. Curr. Opin. Solid State Mater. Sci. 24, 100837 https://doi.org/10.1016/j.cossms.2020.100837.

Daw, M.S., Baskes, M.I., 1984. Embedded-atom method: derivation and application to impurities, surfaces, and other defects in metals. Phys. Rev. B 29, 6443–6453. https://doi.org/10.1103/PhysRevB.29.6443.

Delhommelle, J., Millié, P., 2001. Inadequacy of the lorentz-berthelot combining rules for accurate predictions of equilibrium properties by molecular simulation. Mol. Phys. 99, 619–625. https://doi.org/10.1080/00268970010020041.

Derjaguin, B.V., Muller, V.M., Toporov, Y.P., 1975. Effect of contact deformations on the adhesion of particles. J. Colloid Interface Sci. 53, 314–326. https://doi.org/10.1016/0021-9797(75)90018-1.

Dong, Y., Li, Q., Martini, A., 2013. Molecular dynamics simulation of atomic friction: a review and guide. J. Vac. Sci. Technol. A Vacuum, Surfaces, Film. 31 https://doi.org/10.1116/1.4794357, 030801–030801.

Eberl, C., Spolenak, R., Arzt, E., Kubat, F., Leidl, A., Ruile, W., Kraft, O., 2006. Ultra high-cycle fatigue in pure Al thin films and line structures. Mater. Sci. Eng., A 421, 68–76. https://doi.org/10.1016/j.msea.2005.10.007.

Erkoç, Ş., 2001. Empirical potential energy functions used in the simulations materials properties. In: Annual Reviews of Computational Physics, pp. 1–103. https://doi.org/10.1142/9789812811578_0001.

Fang, T.H., Wu, J.H., 2008. Molecular dynamics simulations on nanoindentation mechanisms of multilayered films. Comput. Mater. Sci. 43, 785–790. https://doi.org/10.1016/j.commatsci.2008.01.066.

Fang, T.H., Chang, W.Y., Huang, J.J., 2009. Dynamic characteristics of nanoindentation using atomistic simulation. Acta Mater. 57, 3341–3348. https://doi.org/10.1016/j.actamat.2009.03.048.

Fincher, C.D., Ojeda, D., Zhang, Y., Pharr, G.M., Pharr, M., 2020. Mechanical properties of metallic lithium: from nano to bulk scales. Acta Mater. 186, 215–222. https://doi.org/10.1016/j.actamat.2019.12.036.

Fischer-Cripps, A.C., 2011. Nanoindentation. Springer. https://doi.org/10.1007/978-1-4419-9872-9.
Foiles, S.M., Baskes, M.I., Daw, M.S., 1986. Embedded-atom-method functions for the fcc metals Cu, Ag, Au, Ni, Pd, Pt, and their alloys. Phys. Rev. B 33, 7983–7991. https://doi.org/10.1103/PhysRevB.33.7983.
Forte, E., Haslam, A.J., Jackson, G., Müller, E.A., 2014. Effective coarse-grained solid-fluid potentials and their application to model adsorption of fluids on heterogeneous surfaces. Phys. Chem. Chem. Phys. 16, 19165–19180. https://doi.org/10.1039/c4cp00670d.
Fu, T., Peng, X., Chen, X., Weng, S., Hu, N., Li, Q., 2016. Molecular dynamics simulation of nanoindentation on Cu/Ni nanotwinned multilayer films using a spherical indenter. Sci. Rep. 6, 35665 https://doi.org/10.1038/srep35665.
Geetha, M., Kumar, N., Panda, K., Dhara, S., Dash, S., Panigrahi, B.K., Tyagi, A.K., Jayavel, R., Kamaraj, V., 2013. Tribological and electrical properties of nanocrystalline Cu films deposited by DC magnetron sputtering with varying temperature. Tribol. Int. 58, 79–84. https://doi.org/10.1016/j.triboint.2012.10.006.
Goel, S., Joshi, S.S., Abdelal, G., Agrawal, A., 2014. Molecular dynamics simulation of nanoindentation of Fe 3 C and Fe 4 C. Mater. Sci. Eng., A 597, 331–341. https://doi.org/10.1016/j.msea.2013.12.091.
Guo, Y., Surblys, D., Kawagoe, Y., Matsubara, H., Liu, X., Ohara, T., 2019. A molecular dynamics study on the effect of surfactant adsorption on heat transfer at a solid-liquid interface. Int. J. Heat Mass Tran. 135, 115–123. https://doi.org/10.1016/j.ijheatmasstransfer.2019.01.131.
Guo, Y., Surblys, D., Matsubara, H., Kawagoe, Y., Ohara, T., 2020. Molecular dynamics study on the effect of long-chain surfactant adsorption on interfacial heat transfer between a polymer liquid and silica surface. J. Phys. Chem. C 124, 27558–27570. https://doi.org/10.1021/acs.jpcc.0c08940.
Guo, Z., Hao, M., Jiang, L., Li, D., Chen, Y., Dong, L., 2020. A modified Hertz model for finite spherical indentation inspired by numerical simulations. Eur. J. Mech./A Solids 83, 104042. https://doi.org/10.1016/j.euromechsol.2020.104042.
Hansson, P., 2015. Influence of the crystallographic orientation and thickness of thin copper coatings during nanoindentation. Eng. Fract. Mech. 150, 143–152. https://doi.org/10.1016/j.engfracmech.2015.08.002.
Hansson, P., 2016. Influence of surface roughening on indentation behavior of thin copper coatings using a molecular dynamics approach. Comput. Mater. Sci. 117, 233–239. https://doi.org/10.1016/j.commatsci.2016.01.042.
Hasnaoui, A., Derlet, P.M., Swygenhoven, H. Van, 2004. Interaction between dislocations and grain boundaries under an indenter – a molecular dynamics simulation. Acta Mater. 52, 2251–2258. https://doi.org/10.1016/j.actamat.2004.01.018.
Herbert, E.G., Pharr, G.M., Oliver, W.C., Lucas, B.N., Hay, J.L., 2001. On the measurement of stress-strain curves by spherical indentation. Mater. Res. Soc. Symp. 649 https://doi.org/10.1557/proc-649-q3.4. Q3.4.1-Q3.4.6.
Hertz, H., 1896. Miscellaneous Papers. MacMillan and Co., London.
Holian, B.L., Ravelo, R., 1995. Fracture Simulations Using Large-Scale Molecular Dynamics 51. https://doi.org/10.1103/PhysRevB.51.11275.
Hu, T.Y., Zheng, B.L., Hu, M.Y., He, P.F., Yue, Z.F., 2015. Molecular dynamics simulation of incipient plasticity of nickel substrates of different surface orientations during nanoindentation. Mater. Sci. Technol. 31 (3), 325–331. https://doi.org/10.1179/1743284714Y.0000000524.
Hu, C., Lv, J., Bai, M., Zhang, X., Tang, D., 2020. Molecular dynamics simulation of effects of nanoparticles on frictional heating and tribological properties at various temperatures. Friction 8, 531–541. https://doi.org/10.1007/s40544-019-0271-9.
Jacobs, T.D.B., Carpick, R.W., 2013. Nanoscale wear as a stress-assisted chemical reaction. Nat. Nanotechnol. 8, 108–112. https://doi.org/10.1038/nnano.2012.255.
Jacobsen, E.H., 1954. Elastic spectrum of copper from temperature-diffuse scattering of X-rays. Phys. Rev. 97, 654–659. https://doi.org/10.1103/PhysRev.97.654.
Jeong, U., Han, J., Marimuthu, K.P., Lee, Y., Lee, H., 2021. Evaluation of mechanical properties of Zr-Cu-Al-Ni TFMG using nanoindentation. J. Mater. Res. Technol. 12, 2368–2382. https://doi.org/10.1016/j.jmrt.2021.04.030.
Jiang, T., Zhu, Y., 2015. Measuring graphene adhesion using atomic force microscopy with a microsphere tip. Nanoscale 7, 10760–10766. https://doi.org/10.1039/C5NR02480C.
Jiang, H., Müller-Plathe, F., Panagiotopoulos, A.Z., 2017. Contact angles from Young's equation in molecular dynamics simulations. J. Chem. Phys. 147, 084708 https://doi.org/10.1063/1.4994088.
Johnson, K.L., 1985. Contact Mechanics. Cambridge University Press. https://doi.org/10.1017/CBO9781139171731.
Johnson, K.L., Greenwood, J.A., 1997. An adhesion map for the contact of elastic spheres. J. Colloid Interface Sci. 192, 326–333. https://doi.org/10.1006/jcis.1997.4984.
Johnson, K.L., Kendall, K., Roberts, A.D., 1971. Surface energy and the contact of elastic solids. Proc. R. Soc. A Math. Phys. Eng. Sci. 324, 301–313. https://doi.org/10.1098/rspa.1971.0141.
Kang, S., Yun, J., Rhee, S., 2002. Microstructure of copper films deposited on TiN substrate by metallorganic chemical vapor deposition. J. Electrochem. Soc. 149, C33–C36. https://doi.org/10.1149/1.1423643.
Kang, S.-K., Kim, Y.-C., Lee, Y.H., Kim, J.-Y., Kwon, D., 2012. Determining effective radius and frame compliance in spherical nanoindentation. Mater. Sci. Eng., A 538, 58–62. https://doi.org/10.1016/j.msea.2012.01.013.
Kimura, R., 1933. Elastic constants of single crystals of cooper. Tohoku Univeristy Rep 22, 553.
Ledbetter, H.M., 1981. Elastic constants of polycrystalline copper at low temperatures. Relationship to single-crystal elastic constants. Phys. Status Solidi A 66, 477–484. https://doi.org/10.1002/pssa.2210660209.
Lennard-Jones, J.E., 1931. Cohesion. Proc. Phys. Soc. 43, 461–482. https://doi.org/10.1088/0959-5309/43/5/301.
Leroy, F., Müller-Plathe, F., 2015. Dry-surface simulation method for the determination of the work of adhesion of solid-liquid interfaces. Langmuir 31, 8335–8345. https://doi.org/10.1021/acs.langmuir.5b01394.
Li, X., Bhushan, B., Takashima, K., Baek, C.-W., Kim, Y.-K., 2003. Mechanical characterization of micro/nanoscale structures for MEMS/NEMS applications using nanoindentation tecniques. Ultramicroscopy 97, 481–494. https://doi.org/10.1016/S0304-3991(03)00077-9.
Li, L., Song, W., Xu, M., Ovcharenko, A., Zhang, G., 2015. Atomistic insights into the loading - unloading of an adhesive contact: a rigid sphere indenting a copper substrate. Comput. Mater. Sci. 98, 105–111. https://doi.org/10.1016/j.commatsci.2014.10.064.
Li, J., Fang, Q., Liu, B., Liu, Youwen, Liu, Yong, 2016. Atomic-scale analysis of nanoindentation behavior of high-entropy alloy. J. Micromechanics Mol. Phys. 1, 1650001 https://doi.org/10.1142/S2424913016500016.
Lin, Q., Zhang, F., Han, F., Zhao, M., Jiang, Z., 2019. Influence of surface roughness on the adhesion hysteresis of nano thin film. Micro & Nano Lett. 14, 1278–1281. https://doi.org/10.1049/mnl.2019.0364.
Liu, T., Liu, G., Xie, Q., Wang, Q.J., 2006. An EFG-FE coupling method for microscale adhesive contacts. J. Tribol. 128, 40–48. https://doi.org/10.1115/1.2114931.
Liu, Y.T., Li, H.M., Gao, M.Z., Ye, S.Q., Zhao, Y., Xie, J., Liu, G.K., Liu, J.J., Li, L.M., Deng, J., Zhou, W.Q., 2021. Experimental and molecular dynamics study into the surfactant effect upon coal wettability. RSC Adv. 11, 24543–24555. https://doi.org/10.1039/d1ra01882e.
Lorentz, H.A., 1881. Ueber die Anwendung des Statzes vom Virial in der kinetischen Theorie der Gase. Ann. Phys. 248, 127–136. https://doi.org/10.1002/andp.18812480110.
Mani, A.Z., Jayadeep, U.B., Ramaseshan, R., 2021. Molecular dynamics simulation of indentation on nanocoated surfaces: a comparison between 3D and 2D plane strain models. J. Mater. Res. 36, 3063–3073. https://doi.org/10.1557/s43578-021-00298-z.
Maugis, D., 1992. Adhesion of spheres: the JKR-DMT transition using a Dugdale model. J. Colloid Interface Sci. 150, 243–269. https://doi.org/10.1016/0021-9797(92)90285-T.
Morales-Rivas, L., González-Orive, A., Garcia-Mateo, C., Hernández-Creus, A., Caballero, F.G., Vázquez, L., 2015. Nanomechanical characterization of nanostructured bainitic steel: peak force microscopy and nanoindentation with AFM. Sci. Rep. 5, 1–16. https://doi.org/10.1038/srep17164.
Müller, E.A., Gubbins, K.E., 1998. Molecular simulation study of hydrophilic and hydrophobic behavior of activated carbon surfaces. Carbon N. Y. 36, 1433–1438. https://doi.org/10.1016/S0008-6223(98)00135-3.
Müller, E.A., Hung, F.R., Gubbins, K.E., 2000. Adsorption of water vapor-methane mixtures on activated carbons. Langmuir 16, 5418–5424. https://doi.org/10.1021/la991312m.
Nair, A.K., Parker, E., Gaudreau, P., Farkas, D., Kriz, R.D., 2008. Size effects in indentation response of thin films at the nanoscale: a molecular dynamics study. Int. J. Plast. 24, 2016–2031. https://doi.org/10.1016/j.ijplas.2008.01.007.
Nair, A.K., Cordill, M.J., Farkas, D., Gerberich, W.W., 2009. Nanoindentation of thin films: simulations and experiments. J. Mater. Res. 24, 1135–1141. https://doi.org/10.1557/JMR.2009.0136.
Neighbours, J.R., Bratten, F.W., Smith, C.S., 1951. The elastic constants of nickel. J. Appl. Phys. 23, 389. https://doi.org/10.1063/1.1702218.
Palacio, M.L.B., Bhushan, B., 2013. Tutorial review Depth-sensing indentation of nanomaterials and nanostructures. Mater. Char. 78, 1–20. https://doi.org/10.1016/j.matchar.2013.01.009.
Perepelkin, N.V., Kovalev, A.E., Gorb, S.N., Borodich, F.M., 2019. Estimation of the elastic modulus and the work of adhesion of soft materials using the extended Borodich–Galanov (BG) method and depth sensing indentation. Mech. Mater. 129, 198–213. https://doi.org/10.1016/j.mechmat.2018.11.017.
Pietrement, O., Troyon, M., 2000. General equations describing elastic indentation depth and normal contact stiffness versus load. J. Colloid Interface Sci. 226, 166–171. https://doi.org/10.1006/jcis.2000.6808.
Raman, C.V., Krishnamurti, D., 1955. Evaluation of the four elastic constants of some cubic crystals. Proc. Indian Acad. Sci. A42, 111–130. https://doi.org/10.1007/BF03053497.
Rassoulinejad-Mousavi, S.M., Mao, Y., Zhang, Y., 2016. Evaluation of copper, aluminum, and nickel interatomic potentials on predicting the elastic properties. J. Appl. Phys. 119, 244304 https://doi.org/10.1063/1.4953676.
Shen, B., Sun, F., 2010. Molecular dynamics investigation on the atomic-scale indentation and friction behaviors between diamond tips and copper substrate. Diam. Relat. Mater. 19, 723–728. https://doi.org/10.1016/j.diamond.2010.01.034.
Shinde, A.B., Patil, S., Patil, P., Salunkhe, R., Sande, R., Pawar, S., Patil, V., 2022. Dislocation and deformation analysis of Cu-Ni thin films during Nano-indentation using molecular dynamics simulation approach. Mater. Today Proc. 49, 1453–1461. https://doi.org/10.1016/j.matpr.2021.07.226.
Sim, Gi-Dong, Krogstad, Jessica A., Reddy, Madhav, Xie, Kelvin Y., Valentino, Gianna M., Weihs, Timothy P., Hemker, Kevin J., 2017. Nanotwinned metal MEMS films with unprecedent strength and stability. Sci. Adv. 3 https://doi.org/10.1126/sciadv.1700685.
Song, Z., Komvopoulos, K., 2013. Elastic – plastic spherical indentation : deformation regimes , evolution of plasticity , and hardening effect. Mech. Mater. 61, 91–100. https://doi.org/10.1016/j.mechmat.2013.01.003.
Song, Tao, Li, D.Y., 2006. Tribological , mechanical and electrochemical properties of nanocrystalline copper deposits produced by pulse electrodeposition. Nanotechnology 17, 65–78. https://doi.org/10.1088/0957-4484/17/1/012.
Stephan, S., Lautenschlaeger, M.P., Alhafez, I.A., Horsch, M.T., Urbassek, H.M., Hasse, H., 2018. Molecular dynamics simulation study of mechanical effects of

lubrication on a nanoscale contact process. Tribol. Lett. 66 https://doi.org/10.1007/s11249-018-1076-0.
Tabor, D., 1977. Surface forces and surface interactions. J. Colloid Interface Sci. 58, 2–13. https://doi.org/10.1016/0021-9797(77)90366-6.
Tang, K.C., Arnell, R.D., 1999. Determination of coating mechanical properties using spherical indenters. Thin Solid Films 356, 263–269.
Teh, W.H., Koh, L.T., Chen, S.M., Xie, J., Li, C.Y., Foo, P.D., 2001. Study of microstructure and resistivity evolution for electroplated copper films at near-room temperature. Microelectron. J. 32, 579–585.
Tersoff, J., 1988. New empirical approach for the structure and energy of covalent systems. Phys. Rev. B 37, 6991–7000. https://doi.org/10.1103/PhysRevB.37.6991.
Tersoff, J., 1989. Modeling solid-state chemistry: interatomic potentials for multicomponent systems. Phys. Rev. B 39, 5566–5568. https://doi.org/10.1103/PhysRevB.39.5566.
Tichy, J.A., Meyer, D.M., 2000. Review of solid mechanics in tribology. Int. J. Solid Struct. 37, 391–400.
Tricoteaux, A., Duarte, G., Chicot, D., Bourhis, E. Le, Bemporad, E., Lesage, J., 2010. Depth-sensing indentation modeling for determination of Elastic modulus of thin films. Mech. Mater. 42, 166–174. https://doi.org/10.1016/j.mechmat.2009.11.016.
Tuck, K., Jungen, A., Geisberger, A., Ellis, M., Skidmore, G., 2005. A study of creep in polysilicon MEMS devices. J. Eng. Mater. Technol. 127, 90–96. https://doi.org/10.1115/1.1839214.
Verlet, L., 1967. Computer "experiments" on classical fluids. I. Thermodynamical properties of Lennard-Jones molecules. J. Phys. D Appl. Phys. 159, 183–195. https://doi.org/10.1088/0022-3727/9/2/008.
Wan, S., Sinclair, R.C., Coveney, P.V., 2021. Uncertainty quantification in classical molecular dynamics. Philos. Trans. R. Soc. A 379, 20200082. https://doi.org/10.1098/rsta.2020.0082.
Wang, Q.J., Zhu, D., 2013. Hertz Theory: Contact of Cylindrical Surfaces, Encyclopedia of Tribology. Springer, Boston, MA. https://doi.org/10.1007/978-0-387-92897-5_491.
Wang, Y.-C., Wu, C.-Y., Chu, J.P., Liaw, P.K., 2010. Indentation behavior of Zr-based metallic-glass films via molecular dynamics simulations. Metall. Mater. Trans. A 41, 3010–3017. https://doi.org/10.1007/s11661-010-0358-4.
Wang, Q., Wu, M., Zhang, C., Lv, Y., Ji, X., 2019. Effect of machining-induced subsurface defects on dislocation evolution and mechanical properties of materials via nano-indentation. Nanoscale Res. Lett. 14 https://doi.org/10.1186/s11671-019-3212-7.
Wu, C., Lin, K., Juang, J., 2016. Hertzian load – displacement relation holds for spherical indentation on soft elastic solids undergoing large deformations. Tribol. Int. 97, 71–76. https://doi.org/10.1016/j.triboint.2015.12.034.
Xu, R.G., Song, H., Leng, Y., Papanikolaou, S., 2021. A molecular dynamics simulations study of the influence of prestrain on the pop-in behavior and indentation size effect in Cu single crystals. Materials 14. https://doi.org/10.3390/ma14185220.
Yang, Z., Zhao, Y.-P., 2007. Adsorption of His-tagged peptide to Ni, Cu and Au (1 0 0) surfaces: molecular dynamics simulation. Eng. Anal. Bound. Elem. 31, 402–409. https://doi.org/10.1016/j.enganabound.2006.07.012.
Yang, B., Zheng, B., Hu, X., Zhang, K., Li, Y., He, P., Yue, Z., 2016. Atomistic simulation of nanoindentation on incipient plasticity and dislocation evolution in Υ/Υ" phase with interface and void. Comput. Mater. Sci. 114, 172–177. https://doi.org/10.1016/j.commatsci.2015.12.021.
Yoon, T., Shin, W.C., Kim, T.Y., Mun, J.H., Kim, T., Cho, B.J., 2012. Direct measurement of adhesion energy of monolayer graphene as- grown on copper and its application to renewable transfer process. Nano Lett. 12, 1448–1452. https://doi.org/10.1021/nl204123h.
Zhang, X., Misra, A., Wang, H., Shen, T.D., Swadener, J.G., Embury, J.D., 2003. Strengthening mechanisms in nanostructured copper/304 stainless steel multilayers. Tribol. Int. 18, 1600–1606. https://doi.org/10.1557/JMR.2003.0220.
Zhu, X., Xu, W., Qin, Y., 2020. Effect of surface tension on the behavior of adhesive contact based on Maugis–Dugdale model. Eur. J. Mech./A Solids 81, 103930. https://doi.org/10.1016/j.euromechsol.2019.103930.